

Perfect Monolayers of the BaTiO₃-Derived 2D Oxide Quasicrystals Investigated by Scanning Tunneling Microscopy and Noncontact Atomic Force Microscopy

Eva Maria Zollner, Sebastian Schenk, Martin Setvin, and Stefan Förster*

The atomic structure of the BaTiO₃-derived 2D oxide quasicrystals (OQCs) is investigated using scanning tunneling microscopy (STM) and noncontact atomic force microscopy (nc-AFM). It is demonstrated that these extraordinary films can easily be prepared as single-phase monolayers on a Pt(111) support. From analyzing almost 20 000 atomic vertices, an extended statistical dataset of the OQC tiling is collected. It manifests that the OQC obeys the statistics of the Niizeki–Gähler tiling, which is a dodecagonal triangle–square–rhomb model system. The atomic structure shown by nc-AFM is identical to the contrast obtained in STM images. The results are discussed with respect to the existing structural models.

1. Introduction

When approaching the 2D limit, oxides are known to exhibit strong variations in their structures and properties compared with the respective bulk materials.^[1] One of most peculiar examples is the 2D oxide quasicrystals (OQCs) formed from ternary oxides on periodic metal substrates which have been reviewed in this issue by Förster et al.^[2–4] Those structures are developed at high temperatures in reducing environment in atomically thin networks on metal supports.^[5] Examples for periodic or aperiodic structures in such 2D layers are found in many systems, e.g., SrTiO₃/Pt(111), BaTiO₃/Pt(111), and BaTiO₃/Ru(0001).^[2,3,6–8] The preparation of OQCs in extended monolayers is challenging, as an exact amount of material needs to be deposited on the

substrate in the correct stoichiometry. Previous reports suffered from this difficulty, and OQCs were found in coexistence with periodic islands formed from excess material. This limited the applications of area-averaging analysis methods and required complex data analysis.^[9] Here, we demonstrate how to succeed in the preparation of perfect monolayers of this new kind material for the case of BaTiO₃/Pt(111). These OQCs films extend across the entire surface, and no material is left to form periodic islands.

We make use of these perfect monolayer templates for structural investigations using a combined scanning tunneling


microscopy (STM)/noncontact atomic force microscopy (nc-AFM). At the atomic level, the structure of the Ti subgrid had previously been resolved by STM.^[2,3] An in-depth analysis of the Ti positions identified the OQC as a disordered Niizeki–Gähler tiling (NGT).^[10–12] In STM, the Ba and O grids are not accessible, due an energetic position of Ba- and O-related bands far from the Fermi level. However, from a combination of STM, surface X-ray diffraction (SXRD) and density functional theory (DFT) calculations performed for a related periodic approximant, a decoration of the triangle and square tiling elements with all three atomic species has been proposed.^[6,7] Based on this model, all Ti atoms are threefold coordinated by O atoms. Furthermore, the sublattice of Ba and some of the O ions should buckle outward of the surface.^[6,7] Therefore, nc-AFM is supposed to be ideally suited for imaging Ba and O ions. However, the constant-height nc-AFM measurements presented here using either metallic or CO functionalized tips show the exactly same contrast as seen in the simultaneously recorded tunneling current images. This implies that the Ti atoms buckle outward from the surface and AFM does not allow to determine the decoration of the dodecagonal tiling by Ba and O.

2. OQC Monolayers on Pt(111)

Perfect monolayers of the BaTiO₃-derived OQCs are fabricated by subsequent deposition of $2.0 \pm 0.1 \text{ \AA}$ of BaO and $2.0 \pm 0.1 \text{ \AA}$ of TiO_x in an oxygen atmosphere of 10^{-6} mbar to the Pt(111) substrate. The deposited material is fully oxidized by annealing in 10^{-5} mbar O₂ for 20 min at 920 K. OQC monolayers are formed by a single 5 min ultrahigh vacuum (UHV) flash of the as-prepared samples at 1100 K. **Figure 1a–d** shows a series of low-energy

E. M. Zollner, S. Schenk, Dr. S. Förster
 Institute of Physics
 Martin-Luther-Universität Halle-Wittenberg
 D-06099 Halle, Germany
 E-mail: stefan.foerster@physik.uni-halle.de

Dr. M. Setvin
 Institute of Applied Physics
 TU Wien
 Wiedner Hauptstraße 8-10/E134, 1040 Wien, Austria

 The ORCID identification number(s) for the author(s) of this article can be found under <https://doi.org/10.1002/pssb.201900620>.

© 2019 The Authors. Published by WILEY-VCH Verlag GmbH & Co. KGaA, Weinheim. This is an open access article under the terms of the Creative Commons Attribution-NonCommercial-NoDerivs License, which permits use and distribution in any medium, provided the original work is properly cited, the use is non-commercial and no modifications or adaptations are made.

DOI: 10.1002/pssb.201900620

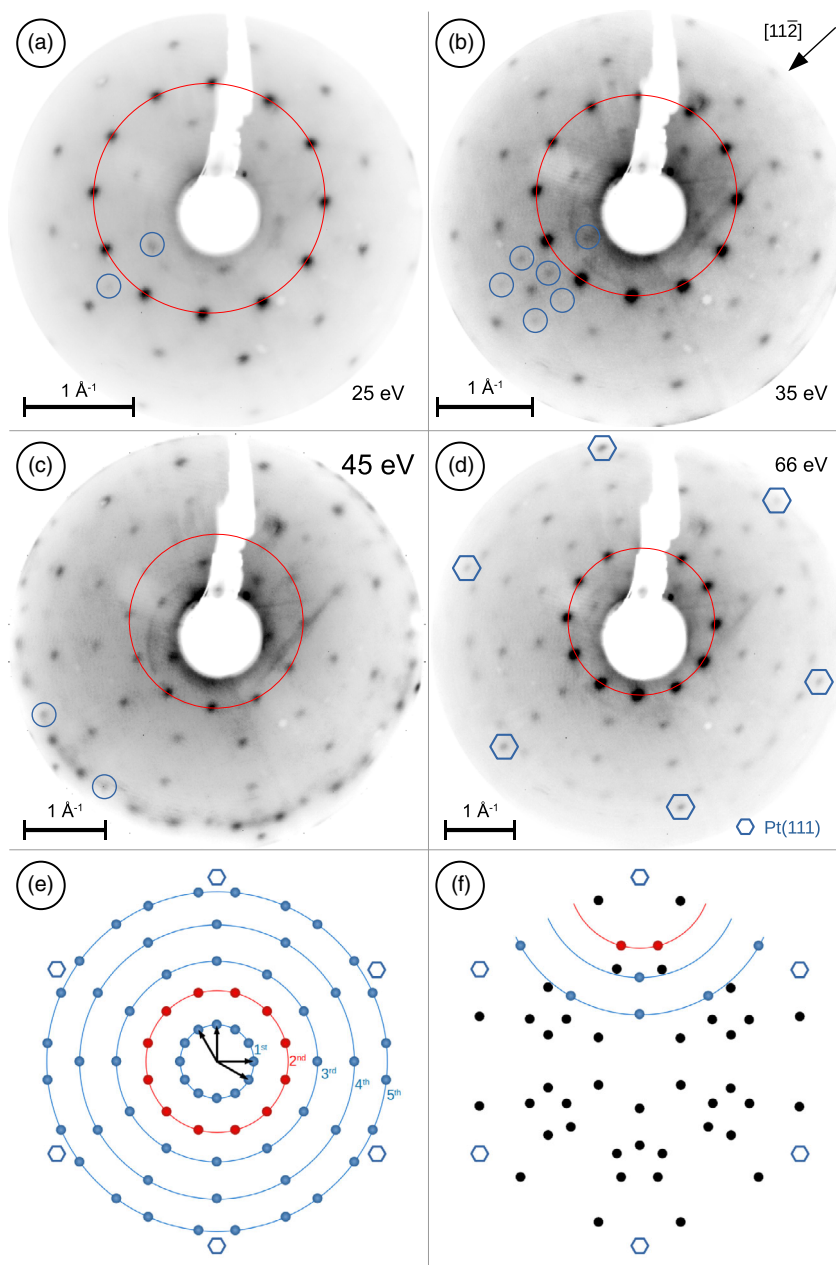


Figure 1. a–d) LEED pattern of the dodecagonal OQC derived from BaTiO₃ on Pt(111) at different kinetic energies. e) The measured data are a superposition of the dodecagonal pattern originating from the first BZ and f) a set of backfolded spots originating from the six neighboring BZs of Pt(111). The backfolded spots along the $[11\bar{2}]$ direction are marked with blue circles in parts (a)–(c).

electron diffraction (LEED) images of the OQC taken at different electron kinetic energies right after this single heating step.

In addition to the Pt(111) substrate spots (marked with hexagons in Figure 1d), all LEED spots are related to the dodecagonal OQC. In the LEED pattern, OQC spots of different origin can be distinguished. The dominating contribution are spots of the dodecagonal structure originating from the first Brillouin zone (BZ). A scheme of such spots is shown in Figure 1e. This pattern represents a 2D projection of a 4D hyperhexagonal lattice, which is the reason for the description with four unit

vectors (black arrows in Figure 1e).^[13] The first-order spots are typically very weak and only observed at energies below 10 eV (not shown here). The most intense feature is the ring of 12 spots corresponding to the second-order of diffraction (red in Figure 1e). For guidance, this order of diffraction is marked in the measured LEED data in red. At larger reciprocal distances, the rings of third- and fourth-order spots appear with 15° rotation against the second-order ring. At the highest electron energy of 66 eV in Figure 1d, additional pairs of fifth-order reflections are observed at every 30°. Theoretically, the reciprocal space of

a OQC consists of an infinitely dense mesh of points, as every point in the 2D space can be approached by the superposition of integer numbers of the four unit vectors. However, for the OQC, only a small number of reflections of nonzero intensity are observed.

The second contribution to the LEED pattern originates from multiple scattering events, which occur at these low electron energies. Electrons that are subsequently scattered at the OQC and the Pt(111) substrate produce additional spots originating from neighboring BZs of the Pt(111) substrate.^[2] This so-called backfolding is schematically shown in Figure 1f. All backfolded spots that have been observed experimentally are drawn here. Each of the neighboring BZs contributes with two second-order reflections (red in Figure 1f), one third-order spot and five spots of the fourth order of diffraction (blue in Figure 1f). In the experimental data, the backfolded spots are exemplary marked along the $[11\bar{2}]$ direction in Figure 1a–c. The superposition of the two contributions shown in Figure 1e,f reduces the symmetry of the observed LEED pattern. The presented OQC pattern extends over the entire sample surface demonstrating an OQC coating of the surface on millimeter scales. Because no additional phase is seen in LEED, the deposited material was completely consumed to form the OQC monolayer.

For atomic-scale characterization using STM and nc-AFM, the sample needed to be transferred through air. To remove adsorbates after re-entering the UHV chamber, the sample has been annealed in 10^{-6} mbar O_2 for 10 min at 920 K. Flashing the sample in UHV afterward to 1100 K for 5 min recovers the OQC structure. Figure 2a shows the homogeneity of the surface in the presence of the OQC layer. On the scale of $200 \times 200 \text{ nm}^2$ flat terraces separated by monoatomic steps are seen. These substrate terraces are completely covered with the OQC layer. Due to its alignment along the high-symmetry substrate directions, the OQC grows as a single-domain overlayer. Accordingly, no domain boundaries are formed on the terraces. The image has been recorded at a resolution of 1500×1500 points, which allows to atomically resolve the OQC structure in the entire area. The Fourier transform of this image is shown in Figure 2b. Twelve intense spots are seen, which correspond to the second-order spots seen in LEED. In addition, higher-order spots at larger and smaller reciprocal distances are resolved. All details of the OQC tiling can be derived from smaller-scale STM images. One example is shown in Figure 2c, which maps a surface region of $40 \times 40 \text{ nm}^2$. In this image, one recognizes the construction principle of the dodecagonal tiling, which is a combination of equilateral triangles, squares, and rhombs. Figure 2c is cut out from a larger dataset and contains about 4000 atomic vertices out of a total number of 19 840. From this large dataset, all atomic positions have been extracted, and a detailed statistical analysis of the atomic tiling has been performed as recently introduced by Schenk et al.^[12] There, it has been shown that the OQC tiling is a first experimentally observed realization of the ideal NGT, which can be constructed by the cut and project method or by recursion.^[10,11,14] The benchmark parameters for this assignment are the total tiling element frequencies and the frequencies of shared edges between adjacent tiles. Schenk et al. conducted this analysis for a system of 8100 atomic vertices and report perfect match between the OQC statistics and that of the ideal NGT. The dataset that is analyzed here is almost a factor of

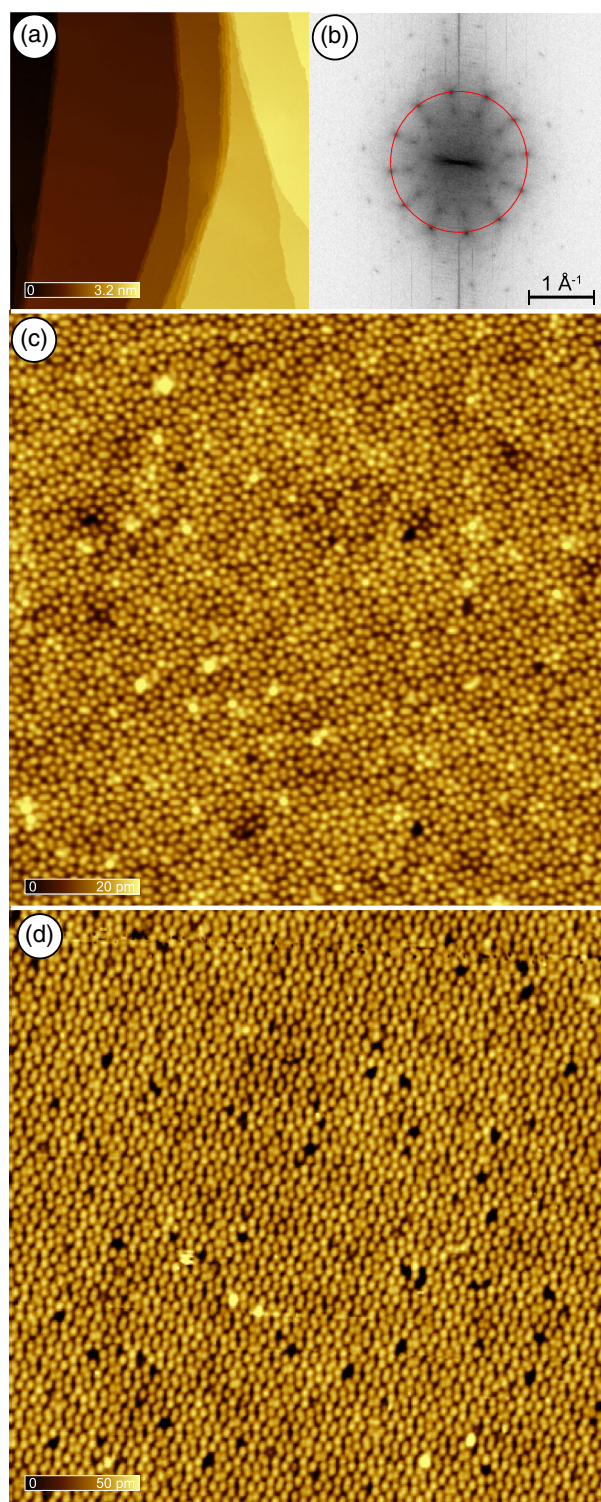


Figure 2. STM data of a perfect monolayer of the $BaTiO_3$ -derived OQC on Pt(111) measured at a–c) 4.8 K and d) at room temperature. a) High-resolution large-scale image showing a homogeneous surface with monoatomic steps covered by the OQC. b) Fourier transform of part (a) on logarithmic scale. Atomic resolution of the OQC structure at c) 4.8 K and d) at room temperature. a) $200 \times 200 \text{ nm}^2$, 30 pA, 0.5 V; c) $40 \times 40 \text{ nm}^2$, 25 pA, 1.0 V; and d) $40 \times 40 \text{ nm}^2$, 100 pA, 1.0 V.

2.5 larger. In total, 19 840 atomic vertices form 19 309 triangles, 7006 squares, and 2634 rhombs, which translates into a triangle:square:rhombs ratio of 2.76:1:0.38. The ideal tiling element ratio of the NGT is 2.73:1:0.37. Only 65 squares are missing in the real system to meet the ideal value, which is less than 1%. The very good match confirms the quasicrystalline nature of the observed tiling. An even stronger benchmark parameter to compare the OQC tiling with the NGT is the frequency of

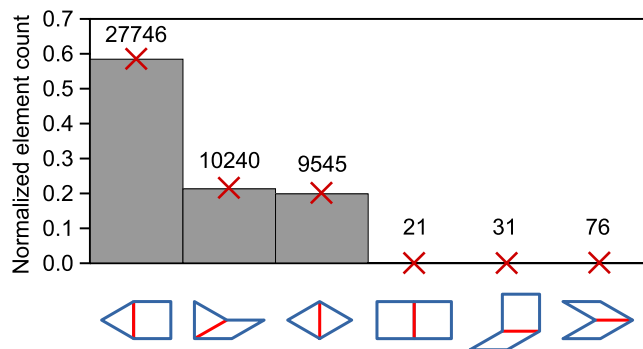


Figure 3. Comparison of the frequencies of shared edges between adjacent tiles in the OQC derived from analyzing 19 840 atomic vertices (red crosses) and the ideal NGT (bars).

shared edges between adjacent tiles, because it reflects the way how the tessellation is created from the different tiles. It will strongly differ from a tiling determined by a recursion rule such as the NGT to, e.g., a random tiling. **Figure 3** shows the comparison of these frequencies for the OQC dataset with those of the NGT.

The agreement is again excellent. Only a minor number of defects is found in the tiling, which are edges shared between two adjacent squares, two rhombs, or a square and a rhomb. Those tiles should not meet in the NGT. However, the total number of such defects is below 0.3%, which means it is negligible. A profound understanding of the observed slight deviations from the ideal tiling configurations and the differences between the OQC preparations analyzed here and published by Schenk et al. would require a proper model for the decoration of tiles with all three atomic species. This is still lacking, which motivated additional nc-AFM measurements as discussed in the following paragraphs.

For the determination of these structural details as derived earlier, the STM measurements do not necessarily need to be performed at liquid helium temperatures. The large interatomic spacing of the Ti atoms of 6.85 Å also allows resolving the structure at room temperature using standard equipment, as shown in **Figure 2d**. From these measurements, all statistical information, as obtained from the low temperature dataset, could

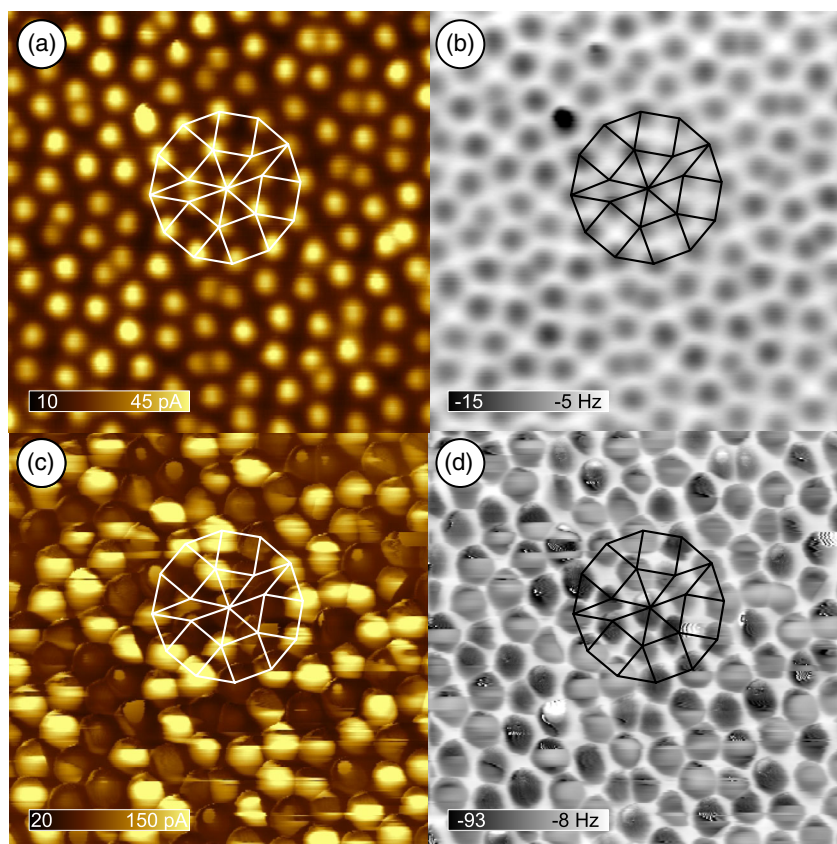


Figure 4. Simultaneously recorded constant-height STM (left column) and nc-AFM images (right column) of the OQC using a metallic tip. One of the characteristic dodecagons of the OQC is emphasized for guidance. $7 \times 7 \text{ nm}^2$, a,b) $U = -0.03 \text{ V}$, $A = 120 \text{ pA}$, c,d) $U = -0.01 \text{ V}$, $A = 60 \text{ pA}$. The tip-sample distance in parts (c) and (d) is 1 Å which is smaller than in parts (a) and (b).

be extracted in a similar fashion with equal precision. The only noticeable difference between this measurement compared with Figure 2c is the slightly increased number of larger dark holes. At these positions, one or two Ti atoms are missing. Such defects are most likely related to preparational issues, e.g., small deviations in the composition, rather than to the measurement temperature.

3. ncAFM Measurements of the OQC Tiling

As the OQC layers do not have an established structural model, nc-AFM measurements have been performed on the aforementioned perfect OQC monolayers with the aim to resolve the cation and anion sublattices. For ionic lattices, AFM can typically show attractive forces above cations and repulsive forces above anions, assuming that the tip apex has a negative electric charge.^[15–18] Positively terminated tips show an inverted contrast.

The nc-AFM measurements presented here have been performed with a variety of tip functionalizations, but the obtained contrast appeared very robust and independent of the tip. **Figure 4** shows typical results obtained with metallic tips. Here, the tip was functionalized by applying voltage pulses above a Cu (001) surface. The AFM images reveal a strong attraction above the atoms that have been identified as Ti by STM. To clearly recognize this, one of the characteristic motifs of the NGT, a dodecagon build from 12 triangles, 5 squares, and 2 rhombs is marked by white lines in the STM image of Figure 4a. At the very same position, the AFM image reveals a dark contrast indicating the attractive tip-sample interaction. Surprisingly, no additional features appear in the frequency shift image of Figure 4b. This observation holds even upon approaching closer to the surface and entering the repulsive regime as shown in Figure 4c,d. The only change in the STM and AFM image contrast is the apparent width of the Ti atoms.

Another frequently used tip functionalization is a CO-tip.^[19] CO was dosed on the surface at $T \approx 60$ K, and the molecule was picked by applying voltage pulses. The tip functionalization was verified by imaging the adsorbed CO molecules. In the AFM image of **Figure 5b**, the adsorbed CO molecules appear as bright spots due to the repulsive CO–CO interaction.^[20] The OQC surface imaged by the CO tip is shown in Figure 5c–h. The sequence of images shows the same spot of the sample at low and medium attractive forces and in the repulsive regime. In comparison with the metallic tip, the maximum attractive forces between the CO tip and the OQC template are somewhat smaller. However, the overall appearance of the OQC tiling remains unchanged. Even in the largest voids of the Ti grid, which are the centers of the squares with a nominal width of 6.85×6.85 nm², no additional features can be identified.

The identical AFM contrast has also been achieved when functionalizing the tip directly at the OQC layer. Such behavior is unusual for ionic surfaces; there, it is typically possible to invert the imaging contrast.^[16,18,21] Also, the magnitude of the frequency shifts obtained on the OQC is significantly higher than typically measured on ionic surfaces. Such robust attractive forces are characteristic for surfaces that form covalent bonds, such as the prototypical silicon surfaces.^[22–24] The domination of the OQC AFM contrast by the Ti atoms independent of the tip

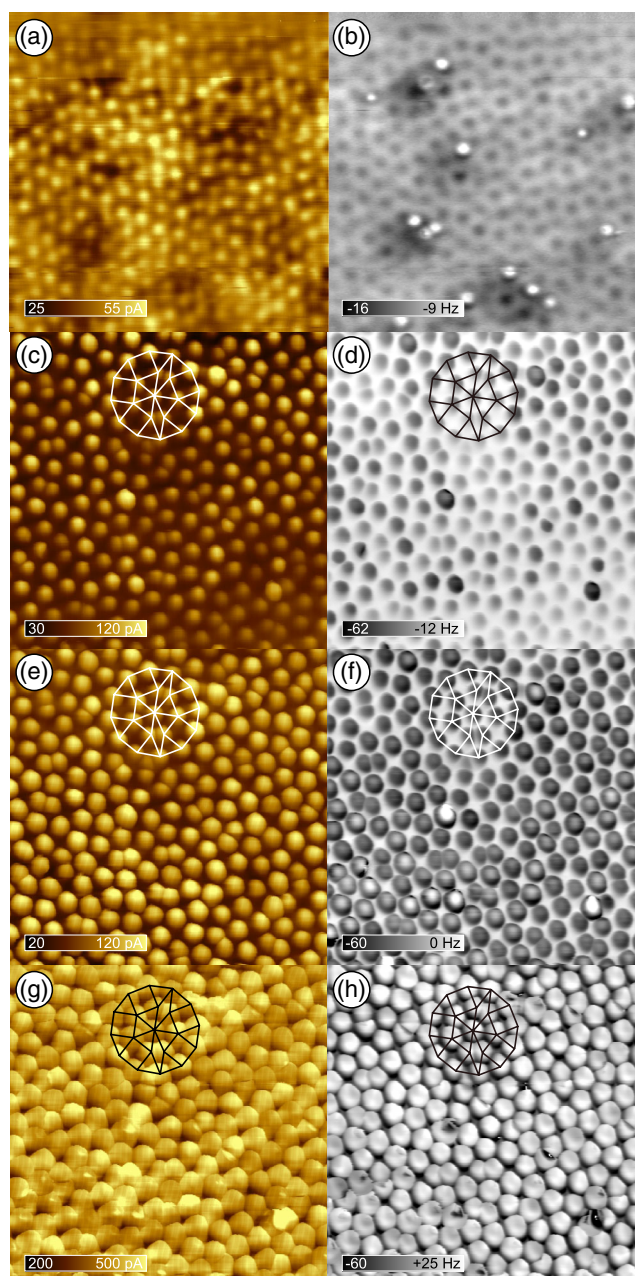


Figure 5. Simultaneously recorded constant-height STM (left column) and nc-AFM images (right column) of the OQC using a CO-terminated tip. One of the characteristic dodecagons of the OQC is emphasized for guidance in parts (c)–(h). a,b) 10×10 nm², $U = +0.04$ V, $A = 60$ pm. The bright spots in the AFM image correspond to the adsorbed CO molecules. c–h) 7×7 nm², $U = +0.002$ V, $A = 50$ pm. The tip-sample distance with respect to parts (a) and (b) is c,d) $\Delta Z = +100$ pm, e,f) $\Delta Z = +190$ pm, and g,h) $\Delta Z = +350$ pm.

configuration suggests a significant outward buckling of the Ti site. Alternatively, it could result from the reduction of the film. In the OQC, the Ti 3d orbitals are singly occupied, as recently shown by valence band photoemission.^[9] This could be the origin of a strongly enhanced reactivity at the Ti sites as seen in AFM.

4. Conclusion

We report on STM and nc-AFM investigations of the BaTiO₃-derived OQC. The AFM data show the identical atomic pattern derived from simultaneously recorded STM images. Previous studies identified these sites as the Ti subgrid of the OQC. The Ti atoms are very dominant in the interaction with AFM tips of different terminations. No other atoms have been detected in the AFM images, even at very close tip-sample distances corresponding to a strongly repulsive interaction. Consequently, the AFM data do not provide a clear lead for solving the OQC structure. However, the high structural quality of single-phase OQC monolayers that is demonstrated here allows for performing surface X-ray standing waves experiments to access the positions of Ba and O atoms in this 2D ternary compound.

5. Experimental Section

Monolayer coverages of BaTiO₃ were prepared on Pt(111) substrates by MBE. BaO and Ti were evaporated in an atmosphere of 10⁻⁶ mbar of O₂ out of a three-pocket electron beam evaporator (EFM3, Omicron). The Ti was supplied from a metal rod and BaO from heating a stoichiometric BaTiO₃ ceramic fixed in a Ta crucible. The deposition rate of each source was routinely calibrated using a quartz-crystal micro balance. After subsequent deposition of a given amount of BaO and TiO_x, the ultrathin oxide film was fully oxidized in 10⁻⁵ mbar O₂ at 920 K for 20 min. The OQC template was prepared by annealing the ultrathin BaTiO₃ film for 5 min at 1100 K in UHV.

The combined STM/AFM experiments were performed at $T = 4.8$ K in an UHV chamber (base pressure $< 2 \times 10^{-11}$ mbar) equipped with a commercial Omicron q-Plus LT head and a custom-design cryogenic preamplifier.^[25] Tuning-fork-based AFM sensors with a separate wire for the tunneling current^[26] were used; $f_0 = 31$ kHz, $Q \approx 20\,000$. Electrochemically etched W tips were glued on the tuning fork and cleaned in situ by field emission and self-sputtering in 10⁻⁶ mbar AR.^[27]

Acknowledgements

The authors gratefully acknowledge the technical support by Ralf Kulla. Financial support was provided from the Deutsche Forschungsgemeinschaft (DFG) through the Collaborative Research Center SFB 762 (Functionality of Oxide Interfaces, project A3). M.S. acknowledges the support from the project FWF P32148-N36.

Conflict of Interest

The authors declare no conflict of interest.

Keywords

atomically resolved STM, dodecagonal tilings, noncontact atomic force microscopy, ternary oxide thin films, tiling statistics, 2D oxide quasicrystals

Received: September 30, 2019

Revised: November 9, 2019

Published online: November 26, 2019

- [1] F. Netzer, S. Fortunelli, *Oxide Materials at the Two-Dimensional Limit*, Springer, Cham **2016**.
- [2] S. Förster, K. Meinel, R. Hammer, M. Trautmann, W. Widdra, *Nature* **2013**, 502, 215.
- [3] S. Schenk, S. Förster, K. Meinel, R. Hammer, B. Leibundgut, M. Paleschke, J. Pantzer, C. Dresler, F. O. Schumann, W. Widdra, *J. Phys.: Condens. Matter* **2017**, 29, 134002.
- [4] S. Förster, S. Schenk, E. M. Zollner, O. Krahn, C.-T. Chiang, F. O. Schumann, A. Bayat, K.-M. Schindler, M. Trautmann, R. Hammer, K. Meinel, W. A. Adeagbo, W. Hergert, J. I. Flege, J. Falta, M. Ellguth, C. Tusche, M. DeBoissieu, M. Muntwiler, T. Greber, W. Widdra, *Phys. Status Solidi B* **2020**, 257, 1900624. (in this issue)
- [5] S. Förster, J. I. Flege, E. M. Zollner, F. O. Schumann, R. Hammer, A. Bayat, K.-M. Schindler, J. Falta, W. Widdra, *Ann. Phys. (Berlin)* **2017**, 529, 1600250.
- [6] S. Förster, M. Trautmann, S. Roy, W. A. Adeagbo, E. M. Zollner, R. Hammer, F. O. Schumann, K. Meinel, S. K. Nayak, K. Mohseni, W. Hergert, H. L. Meyerheim, W. Widdra, *Phys. Rev. Lett.* **2016**, 117, 095501.
- [7] S. Roy, K. Mohseni, S. Förster, M. Trautmann, F. O. Schumann, E. M. Zollner, H. L. Meyerheim, W. Widdra, *Z. Kristallogr.* **2016**, 231, 749.
- [8] E. M. Zollner, F. Schuster, K. Meinel, P. Krause, S. Schenk, B. Allner, S. Förster, W. Widdra, *Phys. Status Solidi B* **2020**, 257, 1900655. (in this issue)
- [9] C.-T. Chiang, M. Ellguth, F. O. Schumann, C. Tusche, R. Kraska, S. Förster, W. Widdra, *Phys. Rev. B* **2019**, 100, 125149.
- [10] N. Niizeki, H. Mitani, *J. Phys. A: Math. Gen.* **1987**, 20, L405.
- [11] F. Gähler, in *Proc. of the ILL/CODEST Workshop*, World Scientific, Singapore, **1988**, p. 13.
- [12] S. Schenk, E. M. Zollner, O. Krahn, B. Schreck, R. Hammer, S. Förster, W. Widdra, *Acta Crystallogr.* **2019**, A75, 307.
- [13] A. Yamamoto, *Acta Crystallogr.* **1996**, A52, 509.
- [14] L.-G. Liao, W.-B. Zhang, T.-X. Yu, Z.-X. Cao, *Chin. Phys. Lett.* **2013**, 30, 026102.
- [15] R. Bechstein, C. Gonzalez, J. Schütte, P. Jelinek, R. Pérez, A. Kuhnle, *Nanotechnology* **2009**, 20, 505703.
- [16] A. Yurtsever, D. Fernandez-Torre, C. Gonzalez, P. Jelinek, P. Pou, Y. Sugimoto, M. Abe, R. Perez, S. Morita, *Phys. Rev. B* **2012**, 85, 125416.
- [17] M. Reticcioli, M. Setvin, X. Hao, P. Flauger, G. Kresse, M. Schmid, U. Diebold, C. Franchini, *Phys. Rev. X* **2017**, 7, 031053.
- [18] M. Ellner, N. Pavlicek, P. Pou, B. Schuler, N. Moll, G. Meyer, L. Gross, R. Perez, *Nanoletters* **2016**, 16, 1974.
- [19] L. Gross, F. Mohn, N. Moll, P. Liljeroth, G. Meyer, *Science* **2009**, 325, 1110.
- [20] M. Reticcioli, I. Sokolovic, M. Schmid, U. Diebold, M. Setvin, C. Franchini, *Phys. Rev. Lett.* **2019**, 122, 016805.
- [21] I. Sokolovic, M. Schmid, U. Diebold, M. Setvin, *Phys. Rev. Mater.* **2019**, 3, 034407.
- [22] F. J. Giessibl, *Science* **1995**, 267, 68.
- [23] Y. Sugimoto, P. Pou, M. Abe, P. Jelinek, R. Perez, S. Morita, O. Custance, *Nature* **2007**, 446, 64.
- [24] M. Emmrich, F. Huber, F. Pielmeier, J. Welker, T. Hofmann, M. Schneiderbauer, D. Meuer, S. Polesya, S. Mankovsky, D. Kodderitzsch, H. Ebert, F. J. Giessibl, *Science* **2015**, 348, 308.
- [25] F. Huber, F. J. Giessibl, *Rev. Sci. Instrum.* **2017**, 88, 073702.
- [26] F. J. Giessibl, *Rev. Sci. Instrum.* **2019**, 90, 01101.
- [27] M. Setvin, J. Javorsky, D. Tucinkova, I. Matolinova, P. Sobotik, P. Kocan, I. Ostadal, *Ultramicroscopy* **2012**, 113, 152.